



1 **Novel insights into deep groundwater exploration by geophysical estimation of**
2 **hard rock permeability**

3 **Muhammad Hasan** ^{1, 2, 3, *}, **Lijun Su** ^{1, 2, 3, **}

4 ¹ *State Key Laboratory of Mountain Hazards and Engineering Resilience, Institute of Mountain*
5 *Hazards and Environment, Chinese Academy of Sciences, Chengdu 610299, China*

6 ² *China-Pakistan Joint Research Center on Earth Sciences, CAS-HEC, Islamabad, Pakistan*

7 ³ *University of Chinese Academy of Sciences, Beijing 100049, China*

8

9 *Corresponding authors:

10 Muhammad Hasan: Email: mhasan@imde.ac.cn; ORCID: [https://orcid.org/0000-0001-6804-](https://orcid.org/0000-0001-6804-7962)

11 [7962](https://orcid.org/0000-0001-6804-7962); Phone Number: +86-13051361710

12 Lijun Su: Email: sulijun1976@163.com; ORCID: <https://orcid.org/0000-0001-9972-4698>

13 Corresponding authors' postal address: State Key Laboratory of Mountain Hazards and
14 Engineering Resilience, Institute of Mountain Hazards and Environment, Chinese Academy of
15 Sciences, Chengdu 610299, China

16

17

18

19

20

21

22



23 **Abstract**

24 Deep groundwater exploration in hard rock is a global challenge. An accurate measurement of
25 hydraulic parameters is essential for both effective groundwater management and the prediction
26 of future scenarios. The permeability (k) of an aquifer is typically measured in groundwater
27 studies. Boreholes are the traditional means of measuring k . However, conventional approaches
28 have a lot of flaws, such as being intrusive, expensive, time-consuming, useful only for areas
29 with relatively uniform topographies, and only providing point-scale k measurements. Moreover,
30 traditional approaches may not be able to do deep groundwater assessments. In contrast,
31 geophysical technologies may assess subsurface hydrogeological conditions across large areas
32 with minimal disruption to existing structures, in a shorter amount of time, and at a reduced cost.
33 Several geophysical investigations previously used empirical methods to estimate the k
34 parameter. These studies, however, used the VES (vertical electrical sounding) method to
35 estimate k in a homogeneous setting at shallow depths, and only in 1D. It is difficult to quantify
36 the aquifer potential in hard rock terrains using borehole or VES-based k due to the intrinsic
37 heterogeneity of the terrain. For the first time, this work uses CSAMT (controlled-source audio-
38 frequency magnetotellurics) method to estimate 2D and 3D k over 1 km depth in the exceedingly
39 diverse environments of different rocks. These findings enable the scientific planning and
40 management of deep groundwater resources in highly varied hard rock terrains where
41 hydrogeological data is unavailable, resulting in a more accurate hydrogeological model
42 compared to prior studies. This, in turn, decreases the necessity for expensive pumping tests and
43 enables a more comprehensive evaluation of aquifer potential.

44 **Keywords:** Permeability (k); Geophysical methods; Hydraulic parameters; Groundwater; Hard
45 rock; Hydrogeological uncertainty



46 **1 Introduction**

47 Metamorphic and igneous rocks make up the bulk of Earth's crust, which accounts for around a
48 third of the planet's surface ([Amiotte Suchet et al., 2003](#)). The main focus of groundwater study
49 in hard rock is the examination of underlying geological layers, faults, and fractures ([Fernando
50 and Pacheco, 2015](#); [Hasan et al., 2021](#)). Groundwater evaluation and monitoring relies heavily
51 on categorizing rock mass according to its aquifer yield, or its capacity to store water ([Majumdar
52 and Das, 2011](#); [Nwosu et al., 2013](#); [Qian et al., 2024](#)). The water-bearing rock's aquifer potential
53 is dependent on a wide range of environmental variables. Several factors influence this, such as
54 the rock type, its relationship and deformation, faults, mineral content, water penetration, rock-
55 rock joints, and the rate of weathering ([Dell'Oca et al., 2020](#); [Abbas et al., 2022](#)). Groundwater
56 evaluations have a major challenge in determining the vertical and horizontal water-holding
57 capacity of underlying rock over expansive areas ([Courtois et al., 2010](#); [Dewandel et al., 2004](#)).
58 Prior to beginning groundwater extraction, it is essential to accurately and thoroughly evaluate
59 the aquifer potential linked to the different types of rock. Structural variability and a lack of data
60 make it difficult to evaluate the water-carrying capabilities of geological layers ([Robinson et al.,
61 2016](#); [Worthington et al., 2016](#); [Zhu et al., 2017](#)). Several groundwater and environmental
62 problems may arise from a lack of understanding of hydrogeological uncertainty ([Dewandel et
63 al., 2004](#); [Refsgaard et al., 2012](#); [Lachassagne et al., 2021](#)). Difficult issues in groundwater
64 research include evaluating the condition of geological layers for continual groundwater
65 assessments and minimizing costs without compromising effectiveness.

66 [Rodell et al. \(2009\)](#), [Wada et al. \(2010\)](#), [Laghari et al. \(2012\)](#), [Wada et al. \(2014\)](#), and
67 [Jasechko et al. \(2024\)](#) all attest to the fact that groundwater resources around the globe are
68 dwindling at an alarming rate. In order to effectively manage and utilize these precious assets, it



69 is crucial to do a thorough and precise assessment of groundwater resources. Consideration of
70 hydraulic properties is crucial in groundwater evaluations. Permeability is the most popular
71 aquifer measure and is mainly used to assess the water-holding capacity of rocks all over the
72 world (Dewandel et al., 2004; Gerke et al., 2011; Allègre et al., 2016; Fiandaca et al., 2018;
73 Mudunuru et al., 2022; Esmailpour et al., 2023; Yan et al., 2024; Carbillet et al., 2024). The
74 aquifer potential of geological layers is usually determined by permeability (Zhang et al., 2004;
75 Pellet et al., 2024). De Lima and Niwas (2000), Soupios et al. (2007), Hasan et al. (2021), and
76 Yang and Zhang (2024) all state that borehole testing is the standard method for measuring
77 aquifer parameters. While boreholes do enhance geological data, producing a comprehensive 2D
78 analysis is a time-consuming and problematic process (Hubbard and Rubin, 2002; Niwas and De
79 Lima, 2003). Borehole methods have a number of drawbacks, including being expensive and
80 time-consuming, requiring large apparatus or machinery, being difficult to implement in hilly
81 terrain, only providing localized information, not being able to image lateral geological
82 structures, and not being able to evaluate the deep subsurface structures (Singh, 2005; Lin et al.,
83 2018; Asfahani, 2023). Uncertainty in the estimation of groundwater resources may result from a
84 lack of borehole data, as these limitations make it challenging to regularly execute a large
85 number of drilling trials. Alternatively, there needs to be a way to reduce the number of
86 expensive drilling while still precisely evaluating the groundwater storage capacity of the
87 potential rock masses.

88 A number of prior groundwater investigations have made use of geophysical techniques
89 (Bentley and Gharibi, 2004; Yadav and Singh, 2007; Fu et al., 2013; Vouillamoz et al., 2014;
90 Robinson et al., 2016; Lin et al., 2018; Kouadio et al., 2020; Abbas et al., 2022; Kouadio et al.,
91 2023; Zhang et al., 2024). A number of studies have shown that geophysical procedures



92 outperform drilling techniques in terms of speed, ease of use, cost, and lack of invasiveness (Hu
93 et al., 2013; Lin et al., 2018; Di et al., 2020; Fusheng et al., 2022; Hasan et al., 2024).
94 Additionally, they are capable of conducting thorough geological evaluations in both the vertical
95 and horizontal planes (Fu et al., 2013; Hasan et al., 2021). These methods are superior to others
96 when it comes to collecting hydrogeological data from various subterranean habitats (Niwas and
97 De Lima, 2003; Wynn et al., 2016; Kouadio et al., 2023). Groundwater studies nowadays often
98 include resistivity surveys. Resistivity methods offer a broader resistivity range compared to
99 other geophysical parameters, which is a major advantage (Bentley and Gharibi, 2004;
100 Camporese et al., 2011; Robinson et al., 2016). The three main methods for measuring resistivity
101 are the controlled source audio-frequency magnetotellurics (CSAMT), vertical electrical
102 soundings (VES), and electrical resistivity tomography (ERT) (Soupios et al., 2007; Di et al.,
103 2020; Zhang et al., 2024). Niwas and De Lima (2003), Soupios et al. (2007), Majumdar and Das
104 (2011), Nwosu et al. (2013), Hasan et al. (2021), and Asfahani (2023) are among the previous
105 groundwater-based geophysical studies that primarily utilized the VES method to evaluate
106 groundwater resources in a single dimension. It is unusual to evaluate aquifer yield at great
107 depths in hard rock terrains using two- and three-dimensional hydraulic properties. Recent
108 studies have demonstrated that CSAMT, which aims to gather extensive subsurface data at very
109 deep depths using 2D/3D evaluations, is the most cost-effective and appropriate geophysical
110 method for researching hard rock (Smith and Booker, 1991; Simpson and Bahr, 2005; Bai et al.,
111 2010; Fu et al., 2013; Hu et al., 2013; Wang et al., 2015; Wynn et al., 2016; Di et al., 2020;
112 Zhang et al., 2021; Kouadio et al., 2023; Hasan et al., 2024). Advantages of CSAMT over other
113 geophysical research methods include its lower cost, its responsiveness to low-resistance rocks,
114 and its ease of usage in challenging topographic circumstances (An et al., 2016; Kouadio et al.,



115 [2020](#); [Zhang et al., 2021](#)). Compared to most geophysical technologies, including ERT,
116 CSAMT's subsurface assessment capabilities are superior due to its depth capacity of up to one
117 kilometer ([Zonge and Hughes, 1988](#); [Hasan et al., 2024](#)). When combined with empirically based
118 methodologies, CSAMT becomes an even more powerful tool for studying the incredibly diverse
119 topographical features.

120 Several factors, such as the type of rock, fault, weathering degree, fluid content,
121 permeability, pore-spacing, fracture, lithology, saturation, and joints, as well as the same
122 structural heterogeneities, determine the geophysical and aquifer characteristics ([Singh, 2005](#);
123 [Sinha et al., 2009](#); [Hasan et al., 2021](#)). Several prior studies utilized geophysical parameters in
124 conjunction with hydraulic data or lithological logs to characterize underlying rock mass units
125 hydrogeologically ([De Lima and Niwas, 2000](#); [Hubbard and Rubin, 2002](#); [Niwas and De Lima,](#)
126 [2003](#); [Singh, 2005](#); [Soupios et al., 2007](#); [Sinha et al., 2009](#); [Majumdar and Das, 2011](#); [Nwosu et](#)
127 [al., 2013](#); [Hasan et al., 2021](#); [Asfahani, 2023](#)). Resistivity methods provide an alternate option for
128 aquifer parameter estimation by creating a beneficial relationship between electrical resistivity
129 and the aquifer parameters (obtained from drilling tests). An innovative aspect of this work is its
130 use of non-invasive geophysical techniques to create two- and three-dimensional k models in a
131 diverse environment with a variety of rock types and significant depths. The planned study will
132 necessitate the boring of a handful of boreholes at key spots all around the project site. A more
133 trustworthy CSAMT study will allow us to evaluate the extensive research area. Then, by
134 directly connecting geophysical and borehole data, k can be established for the entire researched
135 site, even without drilling tests. Two- and three-dimensional k models are generated by applying
136 the resulting equations to the full study area. This approach would reduce the need for costly

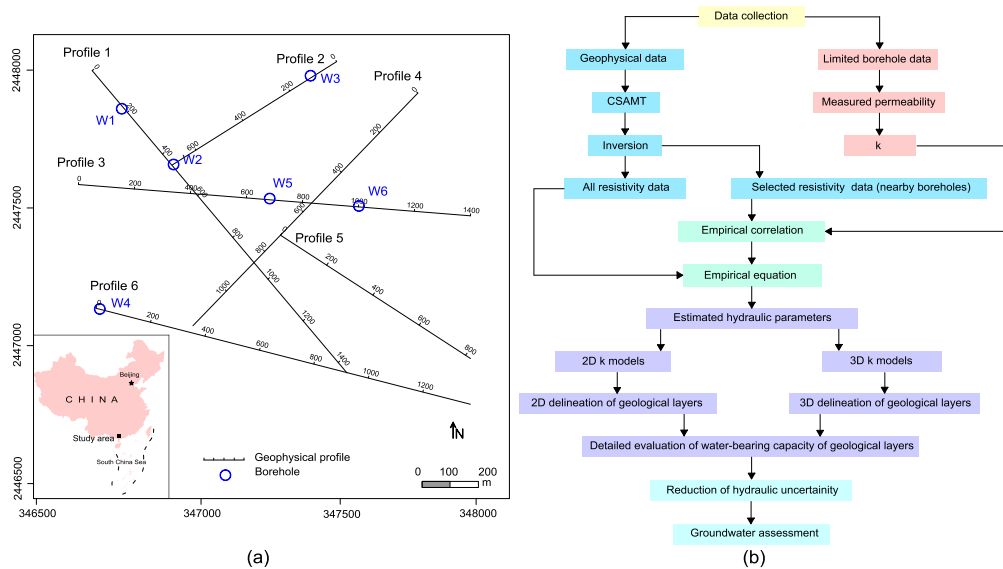


137 boreholes to obtain a thorough and complete evaluation of subsurface hydrogeological
138 conditions.

139 No one had ever tried to estimate K using direct or indirect methods in such a
140 heterogeneous context before this work, where a broad diversity of rock types are present at a
141 depth of 1 kilometer. Volumetric measurements of 2D/3D k have never been obtained in hard
142 rock exploration using a geophysical technique. Furthermore, no previous research has
143 previously derived permeability using the CSAMT method in the same way as this one. Our
144 more precise 2D and 3D k model predictions of complex hydrogeological circumstances surpass
145 prior investigations, bridging the gap between dependable hydraulic models and limited borehole
146 data. The primary goals of this study were as follows: (1) to rapidly predict two- and three-
147 dimensional k models using geophysical methods; (2) to reliably assess the hydrogeological
148 properties of rock formations for deep groundwater assessments in challenging geological
149 settings; (3) to minimize costly boreholes and maximize the use of scarce drilling resources to
150 collect hydrogeological data over large areas; (4) to decrease uncertainties in hydrogeological
151 models; and (5) to promote the use of non-invasive geophysical techniques for hard rock
152 groundwater investigations instead of costly drilling that can damage the rock.

153 **2 Methods**

154 Using existing borehole data and a non-invasive CSAMT method, this study aimed to estimate k
155 for two- and three-dimensional evaluation of groundwater resources over the project area (Fig.
156 1a). A flowchart depicting the primary stages of this method is shown in Fig. 1b.



157

158 **Fig. 1.** (a) The location of the project site, with six boreholes W1–W6 (blue circles) and six CSAMT
159 profiles 1-6 (black lines), (b) Flow diagram outlining the planned method for getting 2D and 3D k models
160 for better, more thorough assessments of groundwater resources over large regions

161 2.1 Study area

162 This study was conducted in the Jinji region of South China to explore deep underground water
163 sources in a geologically diverse area (Fig. 1a). Due to its monsoon location, the study region
164 experiences a concentration of precipitation in the summer, with an annual precipitation totaling
165 1981 mm. Rivers and other water features surround the Jinji area. The geomorphology of the
166 project site is characterized by low, partly cut, and considerably depleted hills and mountains.
167 The terrain in the north is somewhat flatter than that in the south. At a height of 39 to 447 meters
168 above sea level, the region is famous for a number of characteristics, including a wide range of
169 terrain slopes, from gentle to steep, abundant vegetation, and worn mountain rocks (Yang et al.,
170 2021). Noteworthy among these are Mounts Dashishan, Qilongding, and Jixinshan. The southern



171 part of the research area features the 539.9-meter-high Xikeng peak, the landscape's highest point.
172 The Yongkouwei River, which flows through the northeastern part of the site under study at an
173 elevation of around 7.5 meters, cuts through it. Intruding rocks from the Indosinian, Caledonian,
174 and Yanshanian eras are among the many geological formations and periods represented in the
175 study region. Other layers from the Paleogene period are also present. The most common types
176 of rock that have been discovered are sandstone, granite, and hornstone. The complex Kaiping
177 concave fault and fold systems were the dominant geological features in the project region,
178 which were developed as a result of magmatic processes and various structures (Qin, 2017).
179 Emergence of joint fissured features symbolizes the various tectono-geological periods, with the
180 local tectonic line corresponding with the faults strike, especially in the northeast orientation
181 (Yang et al., 2021).

182 **2.2 CSAMT survey**

183 **2.2.1 Principle**

184 The application of CSAMT in the study of hard rock is extensive, as shown in numerous
185 publications (Simpson and Bahr, 2005; Bai et al., 2010; Fu et al., 2013; Wang et al., 2015; Wynn
186 et al., 2016; Di et al., 2020; Zhang et al., 2021; Kouadio et al., 2023; Hasan et al., 2024). For
187 these kinds of studies, a faraway transmitter sends regulated electric signals into the earth, while
188 a receiving station keeps an eye on the electric and magnetic fields (Zonge and Hughes, 1988;
189 Zhang et al., 2021). There is a mathematical relationship between the reflected depth and the
190 frequency in a subsurface structure where different fields have varied propagation depths (Borah
191 and Patro, 2019). By taking advantage of the fact that various rocks have varying electrical
192 conductivities, it tracks variations in the strength of the magnetic field and the main field



193 potential (Cagniard, 1953; Zonge and Hughes, 1988). The signal's frequency components are
194 derived from the time series of the EM field fluctuations using Fourier transforms (Simpson and
195 Bahr, 2005). A field source that is artificially regulated is utilized in CSAMT. Electrodes spaced
196 one to two kilometers apart can be used to measure the electric dipole source's electromagnetic
197 field component. We can set up the wires that will connect the batteries to the current electrodes
198 and the transmitter. The average field source transmitter-receiver distances range from 5 to 10
199 km, though this can vary with depth of investigation (DOI) and geological factors. Dividing the
200 magnitudes of the electric and magnetic fields by two orthogonal directions is one method to find
201 the subsurface resistivity. Fu et al. (2013), Zhang et al. (2021), and Hasan et al. (2024) identified
202 several parameters that impact the resistivity associated with subsurface geology. These factors
203 include fault fragmentation, water saturation, lithological changes in stratigraphic structures,
204 pore fluid, porosity, and rock types. The vertical resolution of 5–20% can be assessed by
205 CSAMT when exploring depths ranging from 20 to 1000 meters. The propagation frequency and
206 subsurface resistivity are the basis of DOI. According to Borah and Patro (2019), a lower
207 frequency and higher resistivity typically result in a higher DOI. The distance between stations
208 determines the lateral resolution; typically, this is between ten and two hundred meters.
209 According to Simpson and Bahr (2005), increasing the distance between stations results in a
210 more robust received signal. At every station, a portable receiver can be used to process, amplify,
211 filter, and record the signal. In order to pick up sent signals, electrode pairs, which include
212 magnetic-field sensors and short grounded dipoles, are utilized. Effective survey planning can
213 reduce the impact of radio transmitters, metal fences, power lines, and other potential sources of
214 inaccurate CSAMT data. Plan, three-dimensional, fence, and cross-sectional views are all
215 potential ways to display the modeled resistivity data.



216 **2.2.2 Data collection**

217 The CSAMT data was acquired using six profiles (1–6) with a 50 meter interval between each
218 station. About 1300 meters was the depth of investigation (DOI) in the CSAMT investigation.
219 We took scalar measurements using the TM Mode. Bidirectional measurements are taken of
220 magnetic and electric field: perpendicular to the measuring line and parallel to it. When doing
221 EMAP observations, the measuring stations must be connected in a sequential fashion and 50 m
222 away from the electrode. We used Gain mode X1 and a 50 Hz linear filter in our arrangement.
223 While the emission current lowers to 2.6–4.5 A at 7680 Hz, it peaks at 12–18 A at 1 Hz. The
224 CSAMT data was collected using a V8 multifunction receiver with a TXU-30 transmitter, which
225 was manufactured in Phoenix, Canada. The TXU-30, a multi-function transmitter with a 30-
226 kilowatt output, may enable an exclusively geophysical approach with transmission voltages up
227 to 1000 V, currents up to 20 A at 1000 V, and currents up to 40 A at 500 V. This GPS-enabled
228 transmitter is ideal for deep investigation since it is compatible with common household three-
229 phase 220 volt alternators. There were 34 separate frequency points utilized, spanning the range
230 of 1–7680 Hz. In addition to collecting data, the V8 multifunction receiver may monitor data
231 sent by other secondary receiving units. The principal receiver's three channels and tracks make
232 this possible. The distances between the transmitter and receiver ranged from 9.3 to 12.5
233 kilometers. The non-polarized electrode was used to record the electric field signals. The signals
234 were picked up by the AMTC-30 inductive sensor, which is designed for high-frequency
235 AMT/CSAMT magnets and operates between 10,000 Hz and 0.1 Hz. We acquired two
236 orthogonal electric field components and three orthogonal magnetic field components at each
237 site, and then we measured the tensor at each location. Here, the information was sourced from
238 the American-made Trimble XH dual-frequency GPS receiver. Using the Hi-Tech V30GNSS



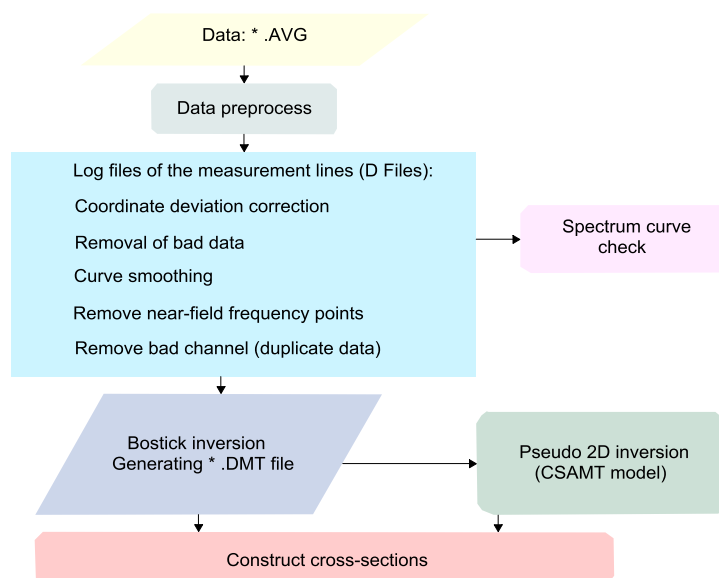
239 RTK apparatus, we measured the CSAMT lines for object recognition. Modern navigational aids
240 allow for pinpoint accuracy on the order of sub-meter precision. The computer calculated the
241 coordinate values of each survey line and survey point using the given direction and distance,
242 and then sent them to the GPS or RTK. We found the measuring points of the survey lines using
243 the RTK or GPS navigational capabilities. The distribution of inspection points was quite
244 consistent when testing them for system quality within a 3–5% range along the measurement
245 lines. The conclusions of the system quality assessment fulfilled the following design criteria: a
246 root-mean-square (RMS) value below $\pm 5\%$, a tolerance for consecutive points on the profile to
247 have an error of less than 10, a tolerance for relative elevation of 1.67mm, and a tolerance for
248 plane of 2.33mm. Because the experiment site was free of human and electrical interference, the
249 data collected was of very high quality. The characteristics of the location were identified by the
250 examination of the CSAMT data (An and Di, 2016; Hasan et al., 2024). Following the
251 elimination of the skewed data, a curve analysis was conducted. The static corrections were
252 made using a Hanning window spatial filtering method, which involved geological information
253 and curve analysis. Correct data processing and interpretation were thus facilitated by the
254 availability of high-quality geophysical data.

255 **2.2.3 Data processing**

256 For the data processing step, we used the CMTPro Version software produced by Phoenix
257 Geophysics (Phoenix Geophysics CMTPro, 2020). This program combines source current,
258 reference track data, and V8 data into CMT files, corrects electrode coordinates, automatically
259 smoothes observed curves, and generates files in the AVG format, among other things. Fig. 2
260 shows a flow diagram of the CSAMT-SW method (Phoenix Geophysics CSAMT-SW, 2020)
261 that was used to conduct the 2D inversion (Rodi and Mackie, 2001; Wang et al., 2015). Here are



262 the main components of the CSAMT-SW: 1. Data translation from AVG to D format; 2. Editing
263 and creating CHK elevation files, and converting them to D format; 3. Manually checking the D
264 file for corrupted sectors, filling in the gaps, removing near-field data, and skipping to certain
265 spots; 4. Inversion outcomes from different static correction methods were very similar when
266 compared; the D file was utilized for smoothing processing; 5. D, H, K, and Z are the four static
267 correction results files for various correction approaches; 6. Converting to text files using
268 BOSTICK inversion and near-field correction; 7. Finite (limited) layers containing data
269 indicating resistivity in depth sections can be created using quasi-2D inversion and the CSAMT
270 global field model (ID), which mixes near and transition fields, applied directly to the measured
271 data from CSAMT. We stored the output as * _BOS.DAT and * _BSS.DAT, respectively, for
272 data in the D file after applying Bostick inversion (Fusheng et al., 2022). The modified data is
273 stored in D files, according to the specifications of the 2D inversion model of CSAMT, in a
274 newly created * _M. DMT text file. Once the maximum number of iterations or RMS error is
275 reached, in this case, 5 iterations, the resulting models are fitted with the observed observations
276 using the inversion approach. A trustworthy 2D resistivity model (Zhang et al., 2021) of CSAMT
277 was produced, considering the local geology and dataset quirks, by employing the most
278 appropriate processing and inversion procedures to reduce model errors. By showing changes in
279 resistivity, the final inversion model improved our knowledge of the subsurface geological
280 characteristics.



281

282 **Fig. 2.** Displaying the procedure of 2D inversion of CSAMT data by the use of Bostick inversion

283 **2.3 Estimation of permeability (k)**

284 In groundwater studies, permeability (k) is frequently employed to identify the groundwater flow
285 characteristics in aquifers (Allègre et al., 2016; Fiandaca et al., 2018; Mudunuru et al., 2022;
286 Esmailpour et al., 2023; Carbillat et al., 2024). Porous materials, such as rocks or
287 unconsolidated materials are characterized by their capacity to permit water to permeate through
288 them. This property is measured by their permeability. An essential factor regulating subsurface
289 flow at any depth is permeability, or the ease with which fluids can pass through porous
290 materials. The permeability of an aquifer is traditionally determined by expensive drilling and
291 laboratory tests. Fluid content, flaws, saturation level, rock composition, faults, compaction,
292 deformation, joints, and cracks are some of the factors that affect permeability (k) (Dewandel et
293 al., 2004; Yan et al., 2024).



294 A large number of researchers have found substantial evidence that geophysical and
295 hydrological features are correlated (De Lima and Niwas, 2000; Hubbard and Rubin, 2002;
296 Niwas and De Lima, 2003; Singh, 2005; Soupios et al., 2007; Sinha et al., 2009; Majumdar and
297 Das, 2011; Asfahani, 2023). The first step in establishing these connections is to calculate the
298 permeability using drilling data collected at certain points. The next step is to integrate the
299 electrical resistivity (using geophysical data) and permeability (measured in boreholes) in order
300 to derive the empirical equations. After that, we put all of the resistivity readings from the six
301 profiles into the resulting equation to get the overall site permeability. This makes it possible to
302 find the site's complete permeability, even when a borehole is inaccessible. In order to provide a
303 one-dimensional estimate of permeability, most of the earlier empirical geophysical approaches
304 relied on vertical electrical sounding (VES), which was most common in uniform settings at
305 shallow depths. As a result, no one had ever used k to probe deep underground water, especially
306 in hard rock formations. We used a CSAMT-based empirical approach to estimate two and three
307 dimensional k across a vast area with different rock formations at great depths for the first time
308 in our recent research.

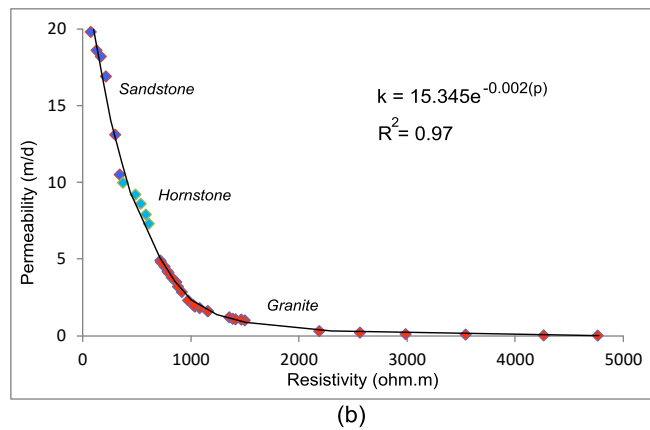
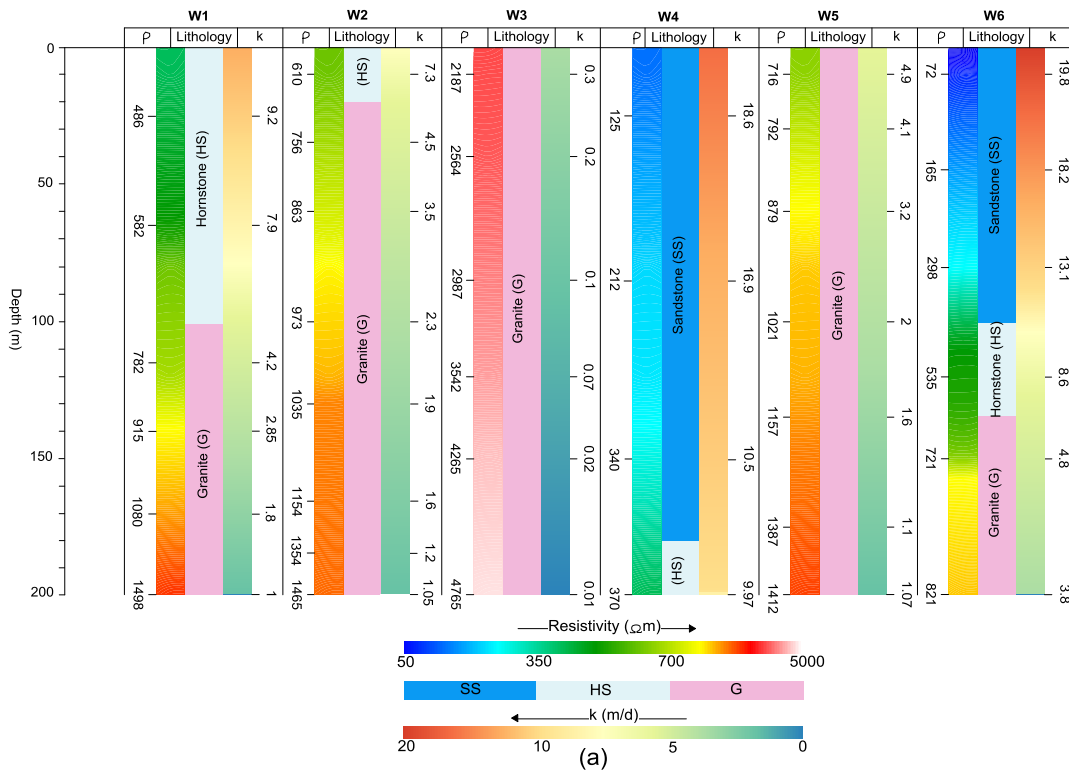
309 Initially, 37 k measurements were obtained from six boreholes (W1, W2, W3, W4, W5,
310 and W6) at varying depths ranging from 10 to 200 meters (Fig. 3a). In the second stage, 37
311 borehole-derived k values were empirically correlated with 37 resistivity values from the chosen
312 CSAMT soundings. P1-5 represents the fifth sounding at 200 meters on surveyed line 1 with
313 well W1; P1-9 denotes the ninth sounding at 400 meters along profile 1 with well W2; P2-3
314 indicates the third sounding at 100 meters with profile 2 and well W3; P6-1 signifies the first
315 sounding at 0 meters on surveyed line 6 with well W4; P3-15 refers to the fifteenth sounding at
316 700 meters along profile 3 with well W5; and P3-21 corresponds to the twenty-first sounding at



317 1000 meters on surveyed line 3 with well W6. In the third stage, the empirical integration of the
318 selected observations (37 data sets) of CSAMT-based resistivity and borehole-based k was
319 utilized to formulate the subsequent equation (Fig. 3b):

$$320 \quad k = 15.345(e)^{-0.002(\rho)} \quad (1)$$

321 where k stands for permeability, which is measured in m/d units, and ρ signifies the true or
322 inverted resistivity, denoted in Ωm . Using comprehensive resistivity data from six geophysical
323 surveyed lines, Eq. (1) was used to predict permeability (k) over the entire area. In this way, we
324 were able to assess the water-retaining capacity of three rock types: granite, hornstone, and
325 sandstone. This allowed us to conduct a thorough evaluation of groundwater resources from 0 to
326 1300 meters below the surface across three potential aquifers: low potential aquifer (LPA)
327 connected to granite, medium potential aquifer (MPA) contained inside hornstone and high
328 potential aquifer (HPA) linked to sandstone). Finally, two- and three-dimensional models were
329 created using the Geosoft and SKUA-GOCAD software tools for the k parameter, a predicted
330 hydrogeological feature that extends throughout all 1-6 geophysical profiles (Webring, 1981;
331 Mira Geoscience Ltd, 1999; Hasan et al., 2024).



332

333 **Fig. 3. (a)** The evaluation of hornstone (HS), sandstone (SS), and granite (G) carried out by presenting 37
 334 resistivity-k data points at depths ranging from 10 to 200 m using 6 drilled tests (W1–W6) and associated
 335 resistivity (ρ) from CSAMT soundings; **(b)** Using a total of 37 data points, the geophysical-borehole
 336 correlation for the predicted k



337 **3 Results**

338 **3.1 Geophysical-borehole correlation**

339 **Table 1** displays the combined data from six boreholes and six CSAMT profiles that were
340 utilized to stratify the underground formation into three distinct layers based on the electrical
341 resistivity and permeability (k) ranges. Data from borehole and CSAMT-based resistivity
342 measurements, as well as the research area's geological context, were used to build the
343 subsurface hydrogeological models. Hornstone, sandstone, and granite are the three separate
344 geological layers that make up these models. When sandstone, hornstone, and granite were being
345 evaluated, the following factors were considered: sandstone's resistivity must be less than 350
346 Ωm and the k range must be between 10 to 20 m/d; hornstone's resistivity must be between 350
347 and 700 Ωm and the k range must be between 5 and 10 m/d; and granite's resistivity must be
348 greater than 700 Ωm and k between 0 and 5 m/d. Based on our evaluations of the subsurface
349 hydrogeological model's aquifer potential zones, we found that sandstone contains the high
350 potential aquifer (HPA), hornstone contains medium potential aquifer (MPA), and granite has
351 low potential aquifer (LPA). Aquifers with the largest yields or the best water-bearing capacity
352 are indicated by sandstone, whereas aquifers with the lowest yields or the worst water-bearing
353 capacities are denoted by granite. Groundwater development is best facilitated by sandstone in
354 the study area, whereas groundwater extraction is most hindered by granite.

355 **Table 1**

356 Integrating the separate ranges of electrical resistivity and permeability (k) allows for a comprehensive
357 evaluation of groundwater in different types of hard rock

Resistivity	k	Type of rock	Aquifer potential
-------------	---	--------------	-------------------



(Ω m)	(m/d)		
< 350	10–20	Sandstone	High potential aquifer (HPA)
350–700	5–10	Hornstone	Medium potential aquifer (MPA)
>700	0–5	Granite	Low potential aquifer (LPA)

358 3.2 2D groundwater assessments

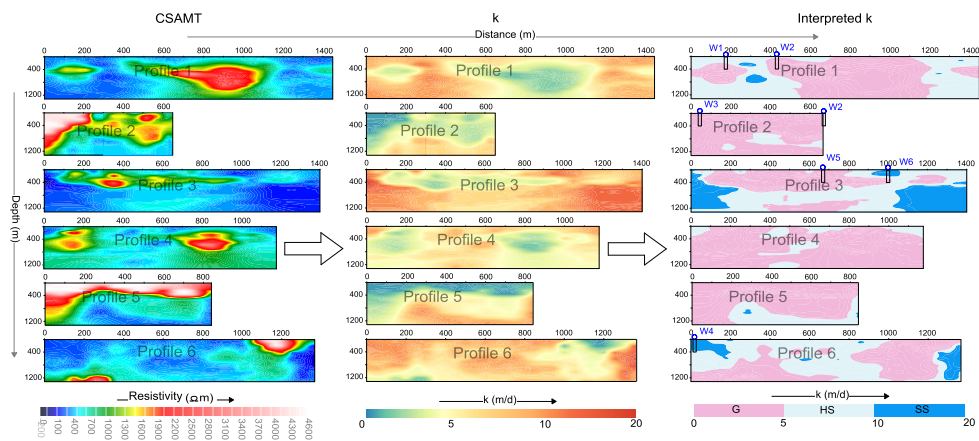
359 Using geophysical-borehole correlation as its basis, Eq. (1) efficiently converts two-dimensional
 360 CSAMT models into two-dimensional k models, as shown in Fig. 4. Fig. 5 and 6 show that, in
 361 contrast to the limited drill experiments, geophysical-based 2D k models allow for an accurate
 362 and comprehensive assessment of the groundwater resources in hard rock across the whole
 363 research area, from 0 to 1300 meters deep. Line 1 of the survey has had the following geological
 364 layers marked out for the purpose of groundwater evaluation: A sandstone layer of high potential
 365 aquifer, 85 to 305 meters thick, is visible between 245 and 380 meters of distance, at depths
 366 ranging from 205 to 400 meters. From 0 to 1300 meters below surface, at concentrations of 0 to
 367 525 meters and 1185 to 1445 meters away, the remaining portion of the profile is composed of a
 368 medium potential aquifer embedded in sandstone. Distances of 0–285 m within 290–790 m depth,
 369 385–1185 m between 0–1300 m depth, and 1305–1450 m within 390–745 m depth were used to
 370 assess granite aquifers with poor potential. Along profile 2, the geological layers that were
 371 employed for groundwater assessment are described as follows: A hornstone layer 140–380
 372 meters thick encloses a medium potential aquifer 490–1105 meters below ground, more precisely
 373 between 145–215 meters and 290–645 meters distance. We did not detect any sandstone
 374 associated with the high potential aquifer along this profile. Along this profile, granite from low
 375 potential aquifers predominates, with the exception of the zones evaluated by medium potential



376 hornstone aquifers; granite is located at 0–700 m distance between 0–1300 m depths. Along
377 profile 3, the following geological layers have been characterized for the purpose of groundwater
378 evaluation: A hornstone-containing medium-potential aquifer is evaluated at depths between 0
379 and 1300 meters and within a range of 0 to 1400 meters distance. Sandstone-associated high
380 potential aquifers are located between 0 and 250 meters distance and between 0 and 1190 meters
381 depths; 905 and 1065 meters away between 0 and 205 meters deep; and 1040 and 1390 meters
382 distance and between 490 and 1305 meters depths. Distances of 80–1015 m between 0–590 m
383 depths, 395–845 m between 915–1300 m depth, and 1100–1300 m between 200–500 m depth are
384 used to assess the possible aquifers contained beneath granite. Here is the breakdown of the
385 geological layers in Profile 4 for the purpose of groundwater assessment: The hornstone medium
386 potential aquifer is checked at distances of 0–105 m and depths of 0–340 m. There is a layer
387 about 290 m thick hornstone at depths ranging from 0 to 1300 m between 340 and 645 m
388 distances, with depths of 0–300 m between 595 and 790 m profile spread, and 0–345 m deep
389 between 1015 and 1145 m distance. No sandstone that could contain a high-potential aquifer is
390 being investigated along this profile. The low potential aquifer associated with granite is
391 delineated at most portions of the profile at 0–1145 m distance between 0–1300 m depths,
392 excluding the areas with medium potential aquifer of hornstone. The geological layers that were
393 considered for the groundwater assessment along profile 5 are as follows: Between 190 and 845
394 meters beneath the granite, there is hornstone associated with a medium-potential aquifer, which
395 is located between 390 and 1325 meters below the surface. Two small sandstone patches of high
396 yield aquifer can also be seen along this profile. One is at a distance of 290 m, between 790 and
397 960 m depth, while the other is at 815 m, between 1045 and 1135 m depth. Within the depth
398 range of 0–1300 meters, granite from low-potential aquifers is assessed at a distance of 0–190

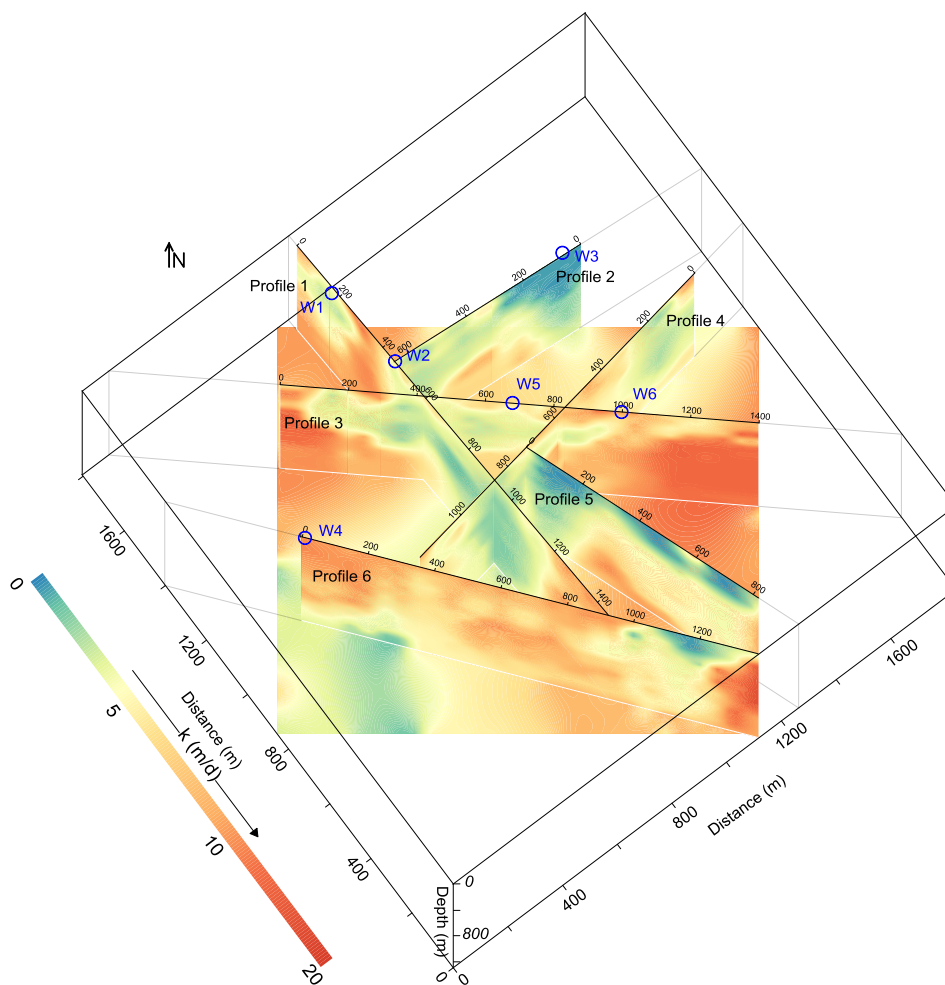


399 meters, and between 0 and 1025 meters, at a distance of 790–815 meters. Here are the geological
 400 layers that can be used for groundwater assessment along profile 6: To assess the high potential
 401 aquifer linked to sandstone, distances of 0–190 m between depths of 0–490 m and 1245–1345 m
 402 between depths of 215–1225 m are utilized. Distances of 0–690 m within depths of 390–1300 m
 403 and 790–1360 m within 0–1190 m depths are used to evaluate low yield aquifer granite. Between
 404 0 and 1300 meters depth and 0 and 1350 meters distance, the hornstone of the medium potential
 405 aquifer dominates the rest of the profile. In the southeastern and northwest regions, there are a lot
 406 of medium to high potential aquifers, according to the results of the integrated 2D k models
 407 shown in Fig. 5 and 6. On the other hand, in the central areas, groundwater resources are scarce
 408 or nonexistent.



409

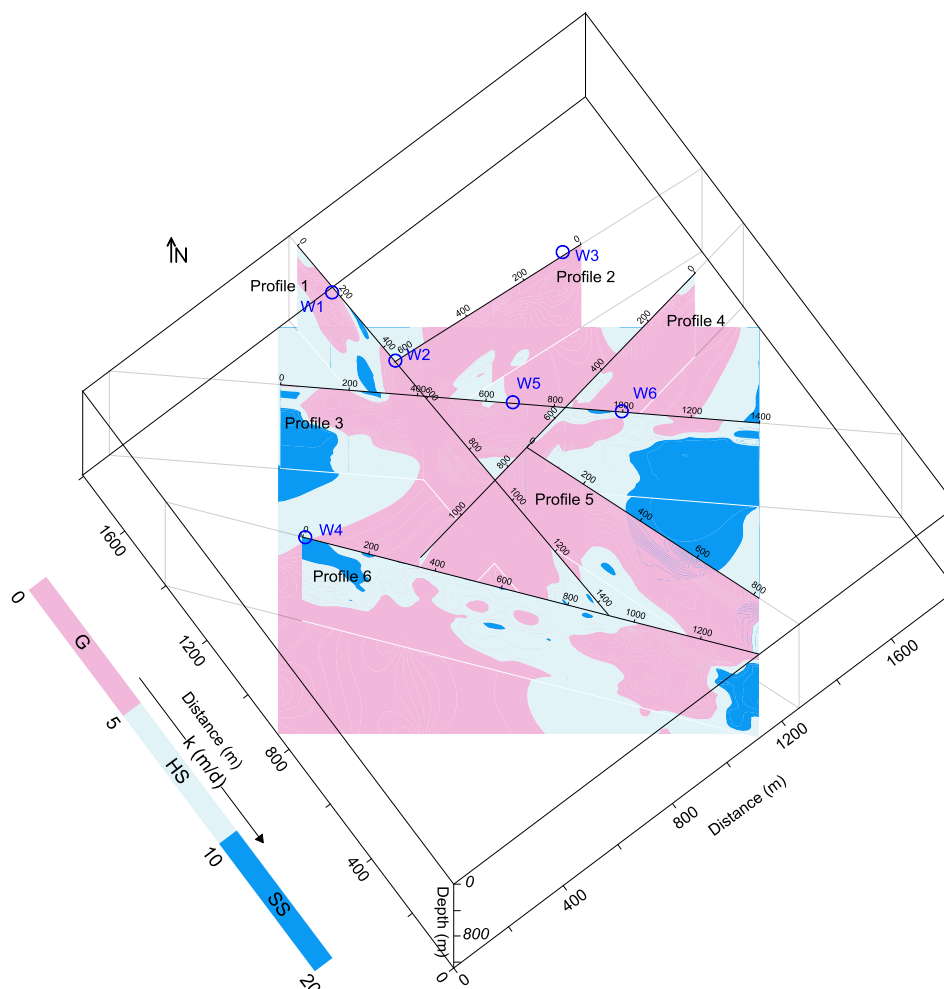
410 **Fig. 4.** The transformation of 2D CSAMT models (for profiles 1–6) into 2D k models, along with the
 411 interpretation of these models via geophysical-borehole correlation, facilitates groundwater assessment
 412 through high potential aquifer (HPA), medium potential aquifer (MPA), and low potential aquifer (LPA)
 413 associated with sandstone (SS), hornstone (HS), and granite (G), respectively



414

415 **Fig. 5.** The integrated 2D k models derived from the incorporation of geophysical and drilling data, with k

416 represented on a color bar spanning from green to red



417

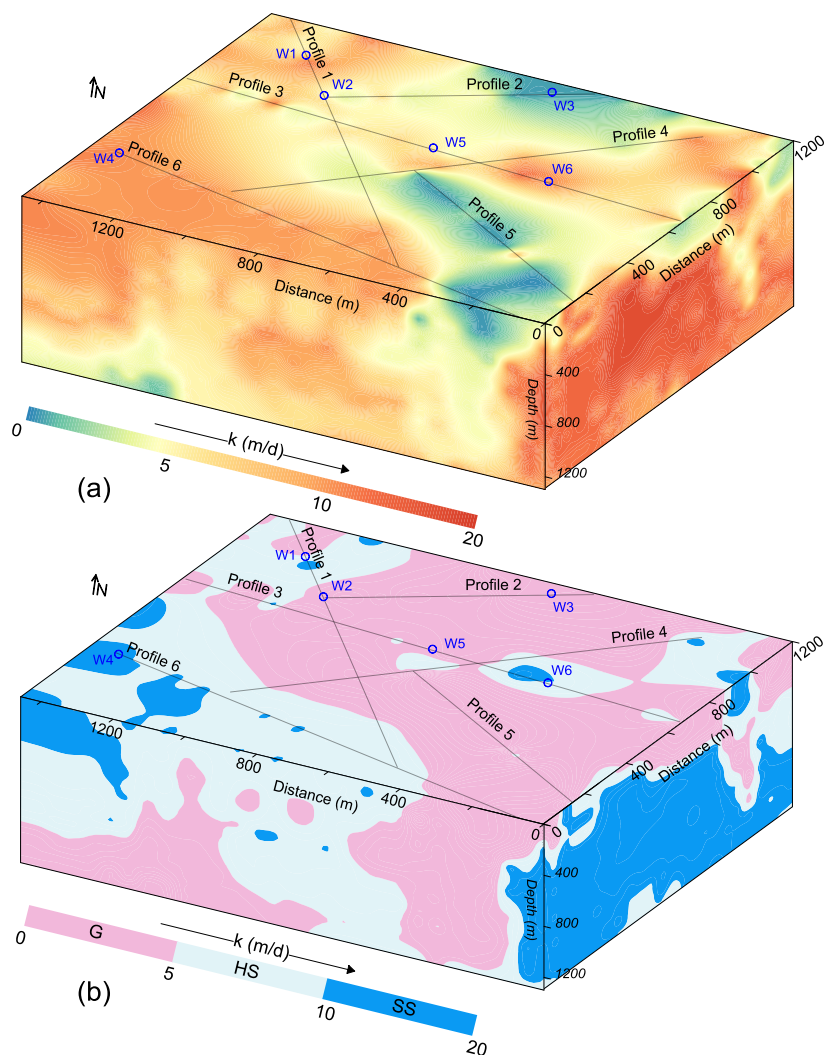
418 **Fig. 6** Analysis of 2D k models (derived from designated k ranges) for three groundwater potential
419 aquifers: low potential aquifer (LPA), medium potential aquifer (MPA), and high potential aquifer (HPA),
420 associated with three geological formations: granite (G), hornstone (HS), and sandstone (SS), respectively

421 3.3 3D groundwater assessments

422 A thorough assessment of the water-bearing capacity of the rock mass for groundwater
423 evaluation was conducted using the 3D k external visualization depicted in Fig. 7 (a, b). The
424 granite of low potential aquifer was evaluated at the ground surface along profile 1 at distances



425 of 85–215 m and 385–1175 m, surveyed line 2 at 0–655 m, CSAMT line 3 at 0–45 m, 95–175 m,
426 265–585 m, 605–845 m, and 1145–1315 m, line 4 at 90–390 m, 490–615 m, and 745–1115 m,
427 line 5 at 0–815 m, and surveyed line 6 at 1045–1345 m. A medium potential aquifer within
428 hornstone was identified along profile 1 at distances of 0–95 m, 190–260 m, 295–415 m, and
429 1185–1425 m; along profile 3 at 40–105 m, 215–275 m, 580–605 m, 850–910 m, 1010–1155 m,
430 and 1310–1410 m; along profile 4 at 45–90 m, 390–490 m, 590–685 m, and 1115–1185 m; and
431 along line 6 at 90–190 m, 215–275 m, 315–485 m, 505–605 m, and 635–1045 m. The sandstone
432 with significant aquifer potential was assessed across many locations: profile 1 at distances of
433 265–310 m, line 3 at 235–255 m and 915–1010 m, profile 4 within 0–45 m, and profile 6 at 0–90
434 m, 210–25 m, 275–305 m, 515–525 m, and 605–635 m. [Fig. 7](#) indicates that elevated aquifer
435 yield is predominantly concentrated in the southern regions.



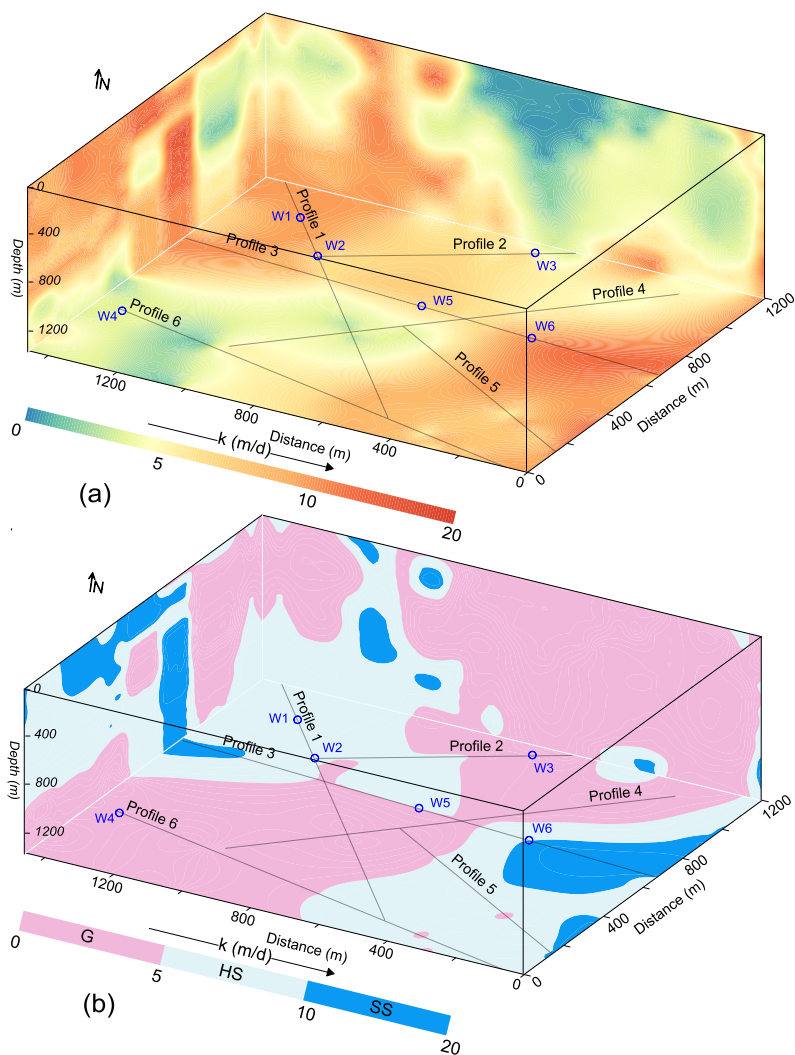
436

437 **Fig. 7.** The 3D k models, generated from the correlation of CSAMT and borehole data (with k represented
438 on a color scale ranging from green to red), correspond to three groundwater potential aquifers: low
439 potential aquifer (LPA), medium potential aquifer (MPA), and high potential aquifer (HPA), associated
440 with three geological strata: granite (G), hornstone (HS), and sandstone (SS), respectively, for (a) the
441 external view of the 3D k model, and (b) the analysis of the 3D k model from an external perspective

442 **Fig. 8** (a, b) presents a comprehensive evaluation of the rock mass's aquifer potential for
443 groundwater assessment using a 3D internal perspective. At a subterranean depth of 1300 m, the



444 low aquifer yield of granite was assessed using profile 1 across a distance of 515–1215 m, profile
445 2 across 0–290 m, profile 3 across 390–690 m, profile 4 across 0–1145 m, profile 5 across 0–195
446 m and 565–595 m, and profile 6 across lengths of 0–695 m and 1075–1115 m. Hornstone
447 associated with a medium potential aquifer was identified by profile 1 at intervals of 0–545 m
448 and 1215–1445 m, profile 2 at 295–675 m, profile 3 at 175–395 m, 445–815 m, and 915–1035 m,
449 profile 5 at 205–565 m and 610–815 m, and surveyed line 6 at 685–1080 m and 1110–1355 m.
450 An aquifer with high potential, situated within sandstone, was evaluated along profile 3 at
451 intervals of 0–205 m and 1010–1400 m, as well as along line 5 at 810–815 m. Medium to high
452 potential aquifers, located at a depth of 1300 m, are predominantly found in the southeastern and
453 northwestern regions, whilst the central areas are primarily characterized by low potential
454 aquifers. [Fig. 8](#) illustrates the results of the 3D K analysis, indicating that the northeastern and
455 southwestern regions are primarily composed of granite with negligible aquifer yield. The water
456 retention capacity of the rock mass is enhanced when observed from an aerial perspective. This
457 enables a precise assessment of the aquifer potential of geological strata for thorough
458 groundwater analysis via 3D k modeling.



459

460 **Fig. 8.** The 3D k models, obtained from the correlation of CSAMT and borehole data (with k represented
461 on a color scale ranging from green to red), illustrate three groundwater potential aquifers: low potential
462 aquifer (LPA), medium potential aquifer (MPA), and high potential aquifer (HPA), associated with three
463 geological strata: granite (G), hornstone (HS), and sandstone (SS), respectively, for (a) the internal view
464 of the 3D k model, and (b) the analysis of the 3D (internal perspective) k model

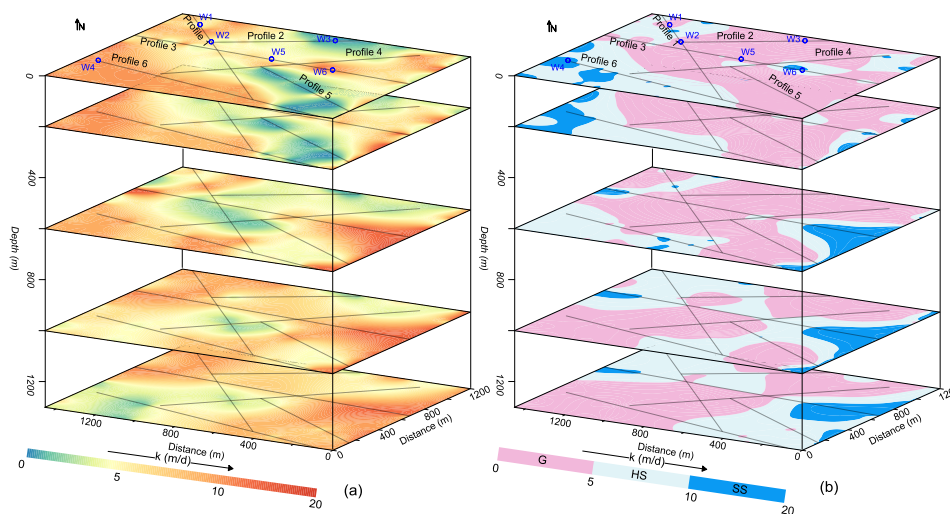
465 3.4 Groundwater assessments via depths



466 Because of the scarcity of borehole data, it is not possible to use the observed k (borehole-based
467 k) to determine the water-bearing capacity of rock masses located below 200 m deep. The
468 evaluation of hard rock groundwater resources was made efficient, precise, and comprehensive
469 by creating a high link between drilling and CSAMT data. Because of this, k could be quickly
470 and accurately determined up to depths of 1300 m. From 2D/3D groundwater yield insights, we
471 were able to derive anticipated k values at 0, 200, 600, 1000, and 1300 m depths (Fig. 9).
472 Evaluation of groundwater at a depth of 1300 meters was based on the following criteria: The
473 southwest and northeastern regions are assessed for granite, which constitutes over 45% of the
474 subsoil in low potential aquifer locations. Near the granite formation in the northwest and
475 southeast, we looked into hornstone, which comprised 40% of the medium potential aquifer. In
476 the eastern region, subsurface assessments were conducted on high-yield sandstone for over 15%
477 of the total. For groundwater evaluation at a depth of 1000 m, the following criteria were used to
478 understand the subsurface: The subsoil around the high-potential aquifers in the southeast
479 consisted of 14% sandstone. Near the granite in the southeast and northwest areas, 38% of the
480 hornstone belonged to a medium-potential aquifer. There were three boundaries, in the middle, to
481 the northeast, and to the southwest, in the subsurface, which was 52% granite and had a poor
482 aquifer yield. We examined the hydrogeological conditions at 600 meters below ground using
483 the following criteria: in the central and northern areas, a low-yielding granite aquifer constituted
484 55% of the subsurface; in the western areas, hornstone was more common, accounting for 32%
485 of the subsurface and indicating a medium-yielding aquifer; and in the southeastern regions,
486 sandstone was the most studied, constituting 13% of the subsoil and indicating a high-yielding
487 aquifer. To assess the hydrogeological conditions at a depth of 200 meters, the following criteria
488 were used: Granite with a low potential aquifer constituted 64% of the total in the center and



489 northern parts. Hornstone with a medium yield aquifer comprised 26% of the underground in the
 490 southern regions. Research in the west focused on sandstone that made up 10% of the subsoil
 491 and had a high potential aquifer. Surface measurements taken at a depth of 0 meters allowed us
 492 to determine the following hydrogeological conditions: While a medium-potential aquifer is
 493 contained within 22% of the southwesterly surface's hornstone, 69% of the subsurface in the
 494 central sections is granite. The sandstone, which is primarily located in the southwest, contains a
 495 high-potential aquifer and is studied on 9% of the surface. Fig. 9 shows that as we descend then
 496 thickness of the granite from low yield aquifers decreases. Midway through, when depth drops to
 497 600 to 700 m, groundwater conditions are at their worst. In the northwest, southeast, and
 498 southwest areas, there are rock masses that could represent aquifers, especially at depths lower
 499 than 700 meters.



500

501 **Fig. 9. (a)** Geophysical k imaging at various depths (0, 200, 600, 1000, and 1300 m) is represented by K
 502 on a color bar that goes from green to red, **(b)** Assessment of geophysical-derived k (using specified k
 503 ranges) at different depths for various types of aquifers: low potential aquifer (LPA) granite (G), medium
 504 potential aquifer (MPA) hornstone (HS), and high potential aquifer (HPA) sandstone (SS)



505 3.5 Comparison of the predicted and measured k

506 Groundwater evaluations across the project area can benefit from the precise and systematic
507 evaluation of water-bearing yield provided by the k generated using CSAMT. Based on the k
508 results (Fig. 4–9), it can be seen that granite is studied in the central, northeastern, and
509 southwestern areas, whereas in the southeastern, western, and northwest regions, hornstone is
510 typically identified as a type of sandstone. Sandstone undergoes extensive analysis in the eastern
511 areas but just minor appraisal in the western sections. It is challenging to evaluate the water-
512 bearing capacity of rock masses using data acquired from boreholes because the resulting
513 incompatible mapping of subsurface geological layers is problematic. Drilling results do match
514 the CSAMT k at a few spots at 200 m deep close to the boreholes. Thus, measured k (obtained
515 via drills) compared to predicted k makes groundwater potential estimations across big regions
516 uncertain.

517 Table 2 presents the percentage of matching for the selected metrics, ascertained by
518 juxtaposing the drill-k with the CSAMT-k. We compared the predicted k with the borehole-
519 based k for several selected data points and observed the following % agreement: Upon
520 experimentally connecting the first well, W1, to the fifth sounding along surveyed line 1 (P1-5),
521 the percentage match at depths of 25 m and 115 m is 85% and 88%, respectively, as per Eq. (1).
522 Following the application of Eq. (1), the percentage matching for sounding 9 along profile 1 (P1-
523 9) and well number two (W2) at a depth of 10 meters and 130 meters, respectively, is 90% and
524 100%. The percentage matching is 70 and 50, respectively, when W3 (well number three) and
525 P2-3 (third sounding on line 2), which have depths of 85 and 150 meters, are merged, as per Eq.
526 (1). We obtain %matching values of 82 and 85, respectively, with depths of 10 and 45 meters, by
527 plugging the data from W4 (the fourth well) and P6-1 (the first sounding at line 6) using Eq. (1).



528 We may acquire %matching of 84 and 85 for depths of 60 and 200 m, respectively, by
 529 integrating W5, the fifth well, and P3-15, the fifteenth sounding at line 3, using Eq. (1).
 530 Additionally, at a depth of 80 and 120 meters, the integration of W6 (well number six) and P3-21
 531 (the 21st sounding on line 3) using Eq. (1) results in a percentage matching of 95 and 85,
 532 respectively. The aforementioned comparison between the obtained and projected k indicates a
 533 lower degree of inaccuracy or strong matching. The comparison also demonstrates that predicted
 534 and measured k values generally fall into the same aquifer potential zone, even for data points
 535 with low %matching.

536 **Table 2**

537 The percentage matching comparison between drill-k and CSAMT-k for the chosen data points

CSAMT data points (selected)			Drilling data			%Matching
CSAMT sounding number	Resistivity (Ωm)	Predicted k' using Eq. (1)	Borehole name	Depth (m)	Measured k	k' vs k
P1-5	486	7.8	W1	25	9.2	85
P1-5	782	3.7	W1	115	4.2	88
P1-9	610	6.6	W2	10	7.3	90
P1-9	1035	1.9	W2	130	1.9	100
P2-3	2987	0.07	W3	85	0.1	70
P2-3	4265	0.01	W3	150	0.02	50
P6-1	72	16.2	W4	10	19.8	82
P6-1	165	15.5	W4	45	18.2	85
P3-15	879	2.7	W5	60	3.2	84
P3-15	1412	0.91	W5	200	1.07	85



P3-21	298	12.5	W6	80	13.1	95
P3-21	535	7.3	W6	120	8.6	85

538 **4 Discussions**

539 Groundwater research is seeing a rise in the use of geophysical technology. Groundwater
540 evaluations have shown promise in prior studies when geophysical and drilling data are
541 combined. We can determine a rock mass's water-bearing potential by looking at its hydraulic
542 properties. Drilling boreholes to measure permeability (k) is the best and most feasible way to
543 measure hydraulic parameters for groundwater evaluations. Through the use of geophysical
544 methods, this study is the first to indirectly obtain 2D/3D k at depths more than 1 km in a context
545 with a diverse range of rocks.

546 This work introduces CSAMT, a novel geophysical method for assessing the water-
547 bearing capacity of rock masses, which allows for more precise groundwater evaluation even
548 when sufficient borehole data is unavailable. This paves the way for a comprehensive assessment
549 of hard rock groundwater at depths above 1 kilometer by means of the anticipated hydraulic
550 parameter k. In light of the varied terrain in southern China, our approach provides a versatile
551 empirical correlation based on the region's massive geophysical dataset and limited drill data.
552 The lithologies and rocks were categorized using the same set of k values as were utilized in the
553 aquifer models. The rocks are classified into three groups based on different aquifer potential
554 zones: fresh granite zone of low potential aquifer (LPA), sandstone zone of high potential aquifer
555 (HPA), and hornstone zone of medium potential aquifer (MPA), which lies in the middle zone
556 between the two possible aquifers. The calculations can be used to find the overall water-bearing
557 capacity of the rock formation in these particular geological settings since they are based on



558 resistivity-k measurements of hornstone, granite, and sandstone. The precise parameter ranges
559 are defined by taking into account the local environment and the rock's composition. The precise
560 rock mass class of a possible aquifer can be determined using the well-established flexible
561 equations, taking into account the hydrogeological conditions of the location. Any geological
562 context can benefit from the generalized equations that can be derived using the suggested
563 method. Because it is relative, a rock unit's k-resistivity range could change depending on are to
564 area. Drilling five or more boreholes across the entire area, with at least five measurements
565 collected from the rock unit in each, usually yields a reliable empirical equation. The reliability
566 of the empirical equation is greatly affected by the ranges of k-resistivity and the quantity of
567 geophysical-borehole datasets. A more precise calculation of k is possible with the use of more
568 datasets in correlation analysis. With real and estimated k matching rates over 80%, most
569 datasets showed an outstanding level of accuracy (Table 2). The established equation provides a
570 poor fit between the anticipated and actual k, especially for very high resistivity and low k values.
571 For instance, the anticipated and calculated k values are in the same LPA zone, even though
572 there was only a 70% and 50% match between W3 and P2-3 at 85 and 150 meters of depth,
573 respectively. All lithologies and rock types, including granite, hornstone, and sandstone, are
574 represented in the resistivity-k ranges used for correlation analysis across the project territory. In
575 order to get trustworthy results, the researchers may have used the drill locations as a proxy for
576 the rock unit characteristics of the whole study site. It may be more accurate to use distinct
577 formulae for each kind of rock unit to find k rather than using a single formula to evaluate
578 several geological layers. While there is sufficient drilling data for each rock mass unit, separate
579 equations may be more effective. Since this correlation is the basis for the expected k, the
580 locations of the surveyed lines are crucial to its correct calculation. As a result, regions near



581 geophysical profiles yield somewhat more accurate findings from two- and three-dimensional k
582 models than regions far from these profiles. We can estimate k in similar geological conditions
583 using the resultant equation when drilling data is not available.

584 CSAMT is heavily utilized for reducing the effect of weak natural signals and for
585 exploring subterranean structures. However, there are a number of factors that might influence
586 resistivity measurements, including transmission devices, electrical lines, metal obstructions, etc.,
587 and this can cause results and interpretations to be unclear. Good CSAMT survey design,
588 however, mitigates these effects and yields accurate results, as demonstrated in this study. Data
589 of a high quality could be collected since the project site was free of electrical and human
590 interference. With a resistivity of 28 Ωm and a k value of 20 m/d, the sandstone rock mass was
591 found to have the highest water-holding capacity. However, the rock mass (granite) was found to
592 have a minimal water-bearing capability of 0.01 m/d when the resistivity value was tested at
593 5000 Ωm . When comparing the geophysical k to the drilling k, the latter provides a more precise
594 and comprehensive evaluation of the rock mass's water-bearing capacity while the former
595 decreases the variability in the anticipated hydrogeological model. Due to a lack of boring trials,
596 hydrogeological models used to evaluate groundwater in highly heterogeneous hard rock are thus
597 profoundly flawed. When hydrogeological models are accurate but borehole data is insufficient,
598 geophysical approaches can help fill the gap.

599 **5 Conclusions**

600 We present new ways to study deep groundwater using non-invasive equipment. To evaluate the
601 water-bearing capacity of rock masses for deep groundwater evaluation across broad, diverse
602 hard rock regions without drilling data, this research applies CSAMT for the first time ever to
603 indirectly estimate two and three dimensional permeability (k) values. In groundwater research,



604 boreholes are the most common method for measuring hydraulic parameters. But drilling
605 methods have a lot of downsides and cost a lot of money. Compared to traditional methods, this
606 study's evaluation of the hydrogeological properties of rock masses is more thorough and precise,
607 and it does so with fewer boreholes. We derived the flexible equation that determines k by
608 examining CSAMT-drilling data from multiple areas in order to evaluate the water-holding
609 capacity of rock formations in varied settings. For groundwater assessment across the entire
610 study area, k was determined using a well-established equation, which allowed for a
611 comprehensive evaluation of the rock mass's water-bearing capacity. With a resistivity below
612 $350 \Omega\text{m}$ and a k range of 10 to 20 m/d, the sandstone of a high potential aquifer (HPA) was
613 studied in a three-layer hydrogeological model. The hornstone of a medium potential aquifer
614 (MPA) was assessed with a resistivity rise ranging from 350 to 700 Ωm and a k range of 5 to 10
615 m/d. The resistivity value of the granite from the low potential aquifer (LPA) was greater than
616 700 Ωm , and the k values were between 0 and 5 m/d. As the resistivity decreases and the k
617 parameter rises, the results show that the rock mass can hold more water. The assumption that
618 sandstone is the rock mass with the greatest water-bearing capacity and granite is the rock mass
619 with the least amount of groundwater was previously thought to underpin the expectations for
620 deep groundwater resources in hard rock. Our 2D/3D k models forecasted that deep groundwater
621 extraction would take place in the center regions at depths below 700 m and in the neighboring
622 areas around granite at depths between 0 and 1300 m. The k -models have been found to have a
623 strong relationship with the hydrogeology and local geology. Based on our findings, this
624 approach has the potential to be a less costly substitute for costly drills in order to obtain more
625 accurate hydrogeological modeling maps than what is now available. When investigating hard
626 rock's groundwater, geophysical methods can evaluate the rock's water-retention capacity rapidly



627 and thoroughly, filling the gap between good hydrogeological models and inadequate drilling
628 data. By utilizing groundwater hydrogeological principles to refine empirical equations, future
629 research could improve the elucidation of aquifer properties. This method would be more useful
630 in groundwater applications since it would enhance our knowledge of how geophysical and
631 aquifer characteristics interact with one another.

632 **Code availability**

633 Software application or custom code supports the published claims and complies with field
634 standards

635 **Data availability**

636 Data available on request from the corresponding author

637 **Author contributions**

638 MH conceptualized the research goals and developed the methodology. MH and LS found the
639 funding for the project. MH developed the code and prepared its visualization, and LS provided
640 programming support and analysis tools. MH prepared the original draft.

641 **Declaration of competing interest**

642 The authors declare that they have no conflict of interest.

643 **Acknowledgements**

644 The authors wish to acknowledge the institutions that facilitated the research for this study: the
645 State Key Laboratory of Mountain Hazards and Engineering Resilience, Institute of Mountain



646 Hazards and Environment, Chinese Academy of Sciences, and China-Pakistan Joint Research
647 Center on Earth Sciences, CAS-HEC, Islamabad, Pakistan.

648 **Financial support**

649 This research was financially supported by the National Natural Science Foundation of China's
650 Research Fund for International Young Scientists (RFIS-I) (Grant No. 42350410442).

651 **References**

- 652 1. Abbas, M., Deparis, J., Isch, A., Mallet, C., Jodry, C., Azaroual, M., Abbar, B., and
653 Baltassat, J.M.: Hydrogeophysical characterization and determination of petrophysical
654 parameters by integrating geophysical and hydrogeological data at the limestone vadose
655 zone of the Beauce aquifer, *Journal of Hydrology*, 615, 128725, 2022.
- 656 2. Allègre, V., Brodsky, E.E., Xue, L., Nale, S.M., Parker, B.L., and Cherry, J.A.: Using
657 earth-tide induced water pressure changes to measure in situ permeability: A comparison
658 with long-term pumping tests, *Water Resour. Res.*, 52, 3113–3126, 2016.
- 659 3. Amiotte Suchet, P., Probst, J.L., and Ludwig, W.: Worldwide distribution of continental
660 rock lithology: Implications for the atmospheric/ soil CO₂ uptake by continental
661 weathering and alkalinity river transport to the oceans, *Glob Biogeochem Cycles*, 17,
662 1038, 2003.
- 663 4. An, Z., and Di, Q.: Investigation of geological structures with a view to HLRW disposal,
664 as revealed through 3D inversion of aeromagnetic and gravity data and the results of
665 CSAMT exploration, *Journal of Applied Geophysics*, 135, 204–211, 2016.



- 666 5. Asfahani, J.: Estimation of the hydraulic parameters by using an alternative vertical
667 electrical sounding technique: case study from semiarid Khanasser valley region
668 Northern Syria, *Acta Geophys*, 71, 997–1013, 2023.
- 669 6. Bai, D., Unsworth, M., Meju, M., Ma, X., Teng, J., Kong, X., Sun, Y., Sun, J., Wang, L.,
670 Jiang, C., Zhao, C., Xiao, P., and Liu, M.: Crustal deformation of the eastern Tibetan
671 plateau revealed by magnetotelluric imaging, *Nature Geosci.*, 3, 358–362, 2010.
- 672 7. Bentley, L.R., and Gharibi, M.: Two- and three-dimensional electrical resistivity imaging
673 at a heterogeneous remediation site, *Geophysics*, 69, 674–680, 2004.
- 674 8. Borah, U.K., and Patro, P.K.: Estimation of the depth of investigation in the
675 magnetotelluric method from the phase, *Geophysics*, 84 (6), E377–E385, 2019.
- 676 9. Cagniard, L.: Basic theory of the magneto-telluric method of geophysical
677 prospecting, *Geophysics*, 18 (3), 605–635, 1953.
- 678 10. Camporese, M., Cassiani, G., Deiana, R., and Salandin, P.: Assessment of local hydraulic
679 properties from electrical resistivity tomography monitoring of a three-dimensional
680 synthetic tracer test experiment, *Water Resources Research*, 47 (12), 2011.
- 681 11. Carbillet, L., Griffiths, L., Heap, M.J., Duwiquet, H., Baud, P., Violay, M.E.S., Reuschlé,
682 T., and Guillou-Frottier, L.: The Influence of Micro- and Macrocracks on the
683 Permeability of Granite, *Rock Mech Rock Eng*, [https://doi.org/10.1007/s00603-024-](https://doi.org/10.1007/s00603-024-04174-0)
684 04174-0, 2024.
- 685 12. Courtois, N., Lachassagne, P., Wyns, R., Blanchin, R., Bougaïre, F.D., Some, S., and
686 Tapsoba, A.: Large-scale mapping of hard-rock aquifer properties applied to Burkina
687 Faso, *Groundwater*, 48 (2), 269–283, 2010.



- 688 13. De Lima, O.A.L., and Niwas, S.: Estimation of hydraulic parameters of shaly sandstone
689 aquifers from geological measurements, *J Hydrol*, 235, 12–26, 2000.
- 690 14. Dell'Oca, A., Guadagnini, A., and Riva, M.: Interpretation of multi-scale permeability
691 data through an information theory perspective, *Hydrol. Earth Syst. Sci.*, 24, 3097–3109,
692 2020.
- 693 15. Dewandel, B., Lachassagne, P., and Qatan, A.: Spatial measurements of stream baseflow,
694 a relevant method for aquifer characterization and permeability evaluation: application to
695 a hard-rock aquifer, the Oman ophiolite, *Hydrol Process*, 18(17), 3391–3400, 2004.
- 696 16. Di, Q., Fu, C., An, Z., Wang, R., Wang, G., Wang, M., Qi, S., and Liang, P.: An
697 application of CSAMT for detecting weak geological structures near the deeply buried
698 long tunnel of the Shijiazhuang-Taiyuan passenger railway line in the Taihang Mountains,
699 *Engineering Geology*, 268, 105517, 2020.
- 700 17. Esmaeilpour, M., Ghanbarian, B., Sousa, R., Peter, R., and King, P.R.: Estimating
701 Permeability and Its Scale Dependence at Pore Scale Using Renormalization Group
702 Theory, *Water Resources Research*, 59 (5), e2022WR033462, 2023.
- 703 18. Fernando, A., and Pacheco, L.: Regional groundwater flow in hard rocks, *Science of the*
704 *Total Environment*, 506–507, 182–195, 2015.
- 705 19. Fiandaca, G., Maurya, P.K., Balbarini, N., Hördt, A., Christiansen, A.V., Foged, N.,
706 Bjerg, P.L., and Auken, E.: Permeability estimation directly from logging-while-drilling
707 induced polarization data, *Water Resources Research*, 54, 2851–2870, 2018.
- 708 20. Fu, C., Di, Q., and An, Z.: Application of the CSAMT method to groundwater
709 exploration in a metropolitan environment, *Geophysics*, 78 (5), 201–B209, 2013.



- 710 21. Fusheng, G., Haiyan, Y., Zengqian, H., Zhichun, W., Ziyu, L., Guocan, W., Linfu, X., Ye,
711 G., and Wanpeng, Z.: Structural setting of the Zoujiashan-Julong'an region, Xiangshan
712 volcanic basin, China, interpreted from modern CSAMT data, *Ore Geology Reviews*, 150,
713 105180, 2022.
- 714 22. Gerke, H.H., Dusek, J., and Vogel, T.: Mass transfer effects in 2-D dual-permeability
715 modeling of field preferential bromide leaching with drain effluent, *Hydrol. Earth Syst.*
716 *Sci. Discuss.*, 8, 5917–5967, 2011.
- 717 23. Hasan, M., Shang, Y., Di, Q., and Meng, Q.: Estimation of Young's modulus for rocks
718 using a non-invasive CSAMT method, *Bulletin of Engineering Geology and the*
719 *Environment*, 83, 464, 2024.
- 720 24. Hasan, M., Shang, Y., Jin, W., and Akhter, G.: Estimation of hydraulic parameters in a
721 hard rock aquifer using integrated surface geoelectrical method and pumping test data in
722 southeast Guangdong China, *Geosci J*, 25 (2), 223–242, 2021.
- 723 25. Hu, X.Y., Peng, R.H., Wu, G.J., Wang, W.P., Huo, G.P., and Han, B.: Mineral
724 exploration using CSAMT data: application to Longmen region metallogenic belt,
725 Guangdong Province, China, *Geophysics*, 78, B111–B119, 2013.
- 726 26. Hubbard, S.H., and Rubin, Y.: Hydrogeological parameter estimation using geophysical
727 data: a review of selected techniques, *J Contam Hydrol*, 45 (3), 34, 2002.
- 728 27. Jasechko, S., Seybold, H., Perrone, D., Fan, Y., Shamsudduha, M., Taylor, R.G., Fallatah,
729 O., and Kirchner, J.W.: Rapid groundwater decline and some cases of recovery in
730 aquifers globally, *Nature*, 625, 715–721, 2024.



- 731 28. Kouadio, K.L., Liu, R., Malory, A.O., and Liu, C.: A novel approach for water reservoir
732 mapping using controlled source audio-frequency magnetotelluric in Xingning area,
733 Hunan Province, China, *Geophysical Prospecting*, 71, 1708–1727, 2023.
- 734 29. Kouadio, K.L., Xu, Y., Liu, C.M., and Boukhalfa, Z.: Two-dimensional inversion of
735 CSAMT data and three-dimensional geological mapping for groundwater exploration in
736 Tongkeng Area, Hunan Province, China, *Journal of Applied Geophysics*, 183, 104204,
737 2020.
- 738 30. Lachassagne, P., Dewandel, B., and Wyns, R.: Review: Hydrogeology of weathered
739 crystalline/hard-rock aquifers—guidelines for the operational survey and management of
740 their groundwater resources, *Hydrogeol J*, 29, 2561–2594, 2021.
- 741 31. Laghari, A.N., Vanham, D., and Rauch, W.: The Indus basin in the framework of current
742 and future water resources management, *Hydrology and Earth System Sciences*, 16 (4),
743 1063–1083, 2012.
- 744 32. Lin, C.H., Lin, C.P., Hung, Y.C., Chung, C.C., Wu, P.L., and Liu, H.C.: Application of
745 geophysical methods in a dam project: Life cycle perspective and Taiwan experience,
746 *Journal of Applied Geophysics*, 158, 82–92, 2018.
- 747 33. Majumdar, R.K., and Das, D.: Hydrological characterization and estimation of aquifer
748 properties from electrical sounding data in Sagar Island region, South 24 Parganas, West
749 Bengal, India, *Asian J Earth Sci*, 4, 60–74, 2011.
- 750 34. Mira Geoscience Ltd.: GOCAD Mining Suite 3D Geological Modeling Software. Nancy
751 University, Lorraine, France, 1999.
- 752 35. Mudunuru, M.K., Cromwell, E.L.D., Wang, H., and Chen, X.: Deep learning to estimate
753 permeability using geophysical data, *Advances in Water Resources*, 167, 104272, 2022.



- 754 36. Niwas, S., and De Lima, O.A.L.: Aquifer parameter estimation from surface resistivity
755 data, *Groundwater*, 41, 94–99, 2003.
- 756 37. Nwosu, L.I., Nwankwo, C.N., and Ekine, A.S.: Geoelectric investigation of the hydraulic
757 properties of the aquiferous zones for evaluation of groundwater potentials in the
758 complex geological area of imostate, Nigeria, *Asian J Earth Sci*, 6, 1–15, 2013.
- 759 38. Pellet, H., Arfib, B., Henry, P., Touron, S., and Gassier, G.: Mesoscale permeability
760 variations estimated from natural airflows in the decorated Cosquer Cave (southeastern
761 France), *Hydrol. Earth Syst. Sci.*, 28, 4035–4057, 2024.
- 762 39. Phoenix Geophysics CMTPro, The Canadian Phoenix CMT Pro Version software for
763 CSAMT data processing. Toronto, Ontario, Canada, 2020.
- 764 40. Phoenix Geophysics CSAMT-SW, The Canadian Phoenix CSAMT-SW Version software
765 for CSAMT data inversion. Toronto, Ontario, Canada, 2020.
- 766 41. Qian, J., Yan, Y., Wang, Y., Liu, Y., Luo, Q.: Effect of scale and matrix porosity on the
767 relationship between permeability and resistivity in fracture-matrix system, *Journal of*
768 *Hydrology*, 629, 130600, 2024.
- 769 42. Qin, X.: Application of Unwedge program to geological stability analysis of deep buried
770 deposits, *Comprehensive*, 8, 270–273, 2017 (In Chinese)
- 771 43. Refsgaard, J.C., Christensen, S., Sonnenborg, T.O., Seifert, D., Højberg, A.L., and
772 Trolborg, L.: Review of strategies for handling geological uncertainty in groundwater
773 flow and transport modeling, *Advances in Water Resources*, 36, 36–50, 2012.
- 774 44. Robinson, J., Slater, L., Johnson, T., Shapiro, A., Tiedeman, C., Ntarlagiannis, D.,
775 Johnson, C., Day-Lewis, F., Lacombe, P., Imbrigiotta, T., and Lane, J.: Imaging



- 776 pathways in fractured rock using three-dimensional electrical resistivity tomography,
777 Groundwater, 54 (2), 186–201, 2016.
- 778 45. Rodell, M., Velicogna, I., and Famiglietti, J.S.: Satellite-based estimates of groundwater
779 depletion in India, Nature, 460 (7258), 999–1002, 2009.
- 780 46. Rodi, W., and Mackie, R.L.: Nonlinear conjugate gradients algorithm for 2-D
781 magnetotelluric inversion, Geophysics, 66 (1), 174–187, 2001.
- 782 47. Simpson, F., and Bahr, K.: Practical magnetotellurics. Cambridge University Press,
783 Cambridge. 254 pp, 2005.
- 784 48. Singh, K.P.: Nonlinear estimation of aquifer parameters from surficial resistivity
785 measurements, Hydrology and Earth System Sciences Discussions, 2 (3), 917–938, 2005.
- 786 49. Sinha, R., Israil, M., and Singhal, D.C.: A hydrogeological model of the relationship
787 between geoelectric and hydraulic parameters of anisotropic aquifers, Hydrogeol J, 17,
788 495–503, 2009.
- 789 50. Smith, J.T., and Booker, J.R.: Rapid inversion of two-and three-dimensional
790 magnetotelluric data, Journal of Geophysical Research: Solid Earth, 96 (B3), 3905–3922,
791 1991.
- 792 51. Soupios, P.M., Kouli, M., Vallianatos, F., Vafidis, A., and Stavroulakis, G.: Estimation of
793 aquifer hydraulic parameters from surficial geophysical methods: a case study of Keritis
794 Basin in Chania (Crete–Greece), J Hydrol, 1, 122–131, 2007.
- 795 52. Vouillamoz, J.M., Lawson, F.M.A., Yalo, N., and Descloitres, M.: The use of magnetic
796 resonance sounding for quantifying specific yield and transmissivity in hard rock aquifers:
797 the example of Beni, J Appl Geophys, 107, 16–24, 2014.



- 798 53. Wada, Y., Van Beek, L.P., Van Kempen, C.M., Reckman, J.W., Vasak, S., and Bierkens,
799 M.F.: Global depletion of groundwater resources, *Geophysical Research Letters*, 37 (20),
800 2010.
- 801 54. Wada, Y., Wisser, D., and Bierkens, M.F.: Global modeling of withdrawal, allocation and
802 consumptive use of surface water and groundwater resources, *Earth System Dynamics*, 5
803 (1), 15–40, 2014.
- 804 55. Wang, R., Yin, C., Wang, M., and Di, Q.: Laterally constrained inversion for CSAMT
805 data interpretation, *Journal of Applied Geophysics*, 121, 63–70, 2015.
- 806 56. Webring, M.W.: MINC: A Gridding Program Based on Minimum Curvature: U.S.
807 Geological Survey Open File Report, 81–1224, p. 41p, 1981.
- 808 57. Worthington, S.R.H., Davies, G.J., and Alexander, E.C. Jr.: Enhancement of bedrock
809 permeability by weathering, *Earth-Sci Rev*, 160, 188–202, 2016.
- 810 58. Wynn, J., Mosbrucker, A., Pierce, H., and Spicer, K.: Where is the hot rock and where is
811 the ground water-using CSAMT to map beneath and around Mount St. Helens, *Journal of*
812 *Environmental and Engineering Geophysics*, 21, 79–87, 2016.
- 813 59. Yadav, G.S., and Singh, S.K.: Integrated resistivity surveys for delineation of fractures
814 for ground water exploration in hard rock areas, *Journal of Applied Geophysics*, 62 (3),
815 301–312, 2007.
- 816 60. Yan, Y., Ma, L., Qian, J., Zhao, G., Fang, Y., Ma, H., and Wang, J.: Estimating
817 permeability of rock fracture based on geometrical aperture using geoelectrical
818 monitoring, *Journal of Hydrology*, 644, 132067, 2024.
- 819 61. Yang, H.Q., and Zhang, L.: Bayesian back analysis of unsaturated hydraulic parameters
820 for rainfall-induced slope failure: A review, *Earth-Science Reviews*, 251, 104714, 2024.



- 821 62. Yang, J., Zhang, H., and Cui, Z.: Stability Analysis and Countermeasures of Rock Block
822 in Underground Cavern, *Guangdong Water Resources and Hydropower* 5, 23–27, 2021
823 (In Chinese)
- 824 63. Zhang, F., Zhou, Z., Huang, Y., and Chen, Z.: Determining the Permeability of Fractured
825 Rocks Based on Joint Mapping, *Groundwater*, 42, 509–515, 2004.
- 826 64. Zhang, J., Sirieix, C., Genty, D., Salmon, F., Verdet, C., Mateo, S., Xu, S., Bujan, S.,
827 Devaux, L., and Larcanché, M.: Imaging hydrological dynamics in karst unsaturated
828 zones by time-lapse electrical resistivity tomography, *Science of the Total Environment*
829 907, 168037, 2024.
- 830 65. Zhang, M., Farquharson, C.G., and Li, C.: Improved controlled source audio-frequency
831 magnetotelluric method apparent resistivity pseudo-sections based on the frequency and
832 frequency–spatial gradients of electromagnetic fields, *Geophysical Prospecting*, 69, 474–
833 490, 2021.
- 834 66. Zhu, L., Gong, H., Dai, Z., Guo, G., and Teatini, P.: Modeling 3-D permeability
835 distribution in alluvial fans using facies architecture and geophysical acquisitions, *Hydrol.*
836 *Earth Syst. Sci.*, 21, 721–733, 2017.
- 837 67. Zonge, K.L., and Hughes, L.J.: *Electromagnetic Methods—Theory and Practice*, 1988.